RSC Advances

PAPER

View Article Online
View Journal | View Issue

Cite this: *RSC Adv.*, 2026, **16**, 26387

A decoupled and scalable solar evaporator integrating boron-enhanced polypyrrole photothermal fabric for efficient water purification

Muneerah Alomar,[a] Lamia Abu El Maati,[a] Muhammad Sultan Irshad,*[b] Naila Arshad,[b] Afraa Alotaibi[a] and Van-Duong Dao *[c]

Interfacial solar evaporation suffers a significant barrier in achieving a balance between significant photothermal efficiency, facile synthesis and long-term stability. Herein, this paper introduces a facile fabrication of functionally decoupled solar evaporation design that addresses this problem by strategic layer separation. For this, polypyrrole coatings of boron nanoparticle (B@PPy) is successfully carried out by scalable *in situ* polymerization for the construction of efficient photothermal materials. This scalable process was employed to cotton fabric (B@PPy) to construct a decoupled solar evaporator, thermally isolated by a polyethylene terephthalate (PET) foam, effectively minimizing parasitic heat loss. Importantly, a separate, unmodified white cotton cloth acts as a specific water transport pathway, wicking water directly from a reservoir to the evaporation interface without affecting the photothermal surface. This decoupled design, which physically separates light absorption, thermal insulation, and water supply, allows for excellent thermal localization. Under 1 sun irradiation, the evaporator achieves a high evaporation rate of 1.90 kg m^{-2} h^{-1} with a solar-thermal conversion efficiency of 92.5%. This study presents a scalable, material-efficient, and architecturally sophisticated approach for high-performance, maintenance-free solar desalination, paving the way for viable off-grid water purification solutions.

Received 27th March 2026
Accepted 13th May 2026

DOI: 10.1039/d6ra02531e

rsc.li/rsc-advances

1. Introduction

Sustainable development and human well-being are seriously threatened by the growing global water scarcity, exacerbated by population growth, industrialization, and climate change.[1] Although water covers more than 70% of the Earth's surface, most of it is salty and unsuitable for direct consumption or agricultural use. As a result, desalination technologies are now more important for producing freshwater.[2] Reverse osmosis and multi-stage flash distillation are two forms of conventional desalination techniques that are quite effective but are still energy-intensive, require a large infrastructure, and have high operating costs, making them inaccessible in distant and undeveloped areas.[3] Additionally, treating wastewater polluted with heavy metal ions and other contaminants poses a different but equally urgent problem that demands effective and affordable remediation techniques.[4] These constraints have accelerated the quest for decentralized, affordable, and sustainable water purification systems. Solar-driven interfacial evaporation (SDIE) has become one of the more intriguing choices.[5] SDIE systems avoid bulk water heating and achieve great energy efficiency by accurately localizing solar-to-thermal energy conversion at the air–water interface.[6] This method makes use of clean, abundant solar energy, providing an off-grid, potentially sustainable desalination and wastewater treatment solution with a far lower carbon impact.[7]

The photothermal material, which is responsible for collecting sunlight and turning it into heat, is the fundamental part of an effective SDIE system. Different photothermal materials have been investigated, including semiconductors, conjugated polymers, carbon-based materials (such as graphene and carbon nanotubes),[8,9] and plasmonic metals (such as Au and Ag nanoparticles).[10,11] Despite their promising performance, many face inherent limitations, such as balancing high photothermal conversion with other properties like mechanical stability or effective salt rejection. In a flexible heater, for example, an MXene@PPy layer produced a 51.61% transmittance to reach a temperature of 47.5 °C after one solar irradiation.[12] Although MXene-based composites have great performance, obtaining this coupled with high transparency remains challenging. Moreover, ongoing difficulties include salt deposition and long-term mechanical stability in adverse saline conditions. Even though three-dimensional (3D) evaporators, such as tubular PPy

[a]*Department of Physics, College of Science, Princess Nourah bint Abdulrahman University, P.O. Box 84428, Riyadh 11671, Saudi Arabia*

[b]*Ministry of Education Key Laboratory of Green Preparation and Application for Functional Materials, School of New Energy and Electrical Engineering, Hubei University, 430062 Wuhan, China. E-mail: muhammadsultanirshad.hubu.edu.cn*

[c]*Faculty of Biotechnology, Chemistry, and Environmental Engineering, Phenikaa School of Engineering, Phenikaa University, Hanoi 12116, Vietnam. E-mail: duong.daovan@phenikaa-uni.edu.vn*

integrated onto biomass foam, can resist salt fouling in 7% brine and achieve high evaporation rates (~1.8 kg m^{-2} h^{-1}), they still experience significant salt accumulation in hypersaline conditions unless they are supported by an additional foam matrix.[13] This emphasizes the necessity of designs that naturally combine strong salt-rejection capabilities with effective light absorption. Boron offers a distinct combination of photothermal characteristics that outperform traditional materials like carbon black, graphene, gold nanoparticles, and polydopamine. In contrast to carbon-based materials, which experience gradual oxidation and diminished performance with prolonged exposure to solar radiation, amorphous boron demonstrates remarkable thermal stability with a melting point above 2000 °C, guaranteeing long-lasting and reliable steam generation during extended use. When compared to noble metal plasmonic absorbers (such as Au, Ag, and Pt), which necessitate intricate nanostructuring and come with high material costs, boron is abundant in nature and economically advantageous while still exhibiting strong photothermal conversion performance. Additionally, unlike organic photothermal polymers like polypyrrole or polydopamine that may photobleach or deteriorate under intense sunlight, boron remains chemically stable and retains photostability. Integrating boron with polypyrrole (PPy)[14–16] effectively merges the structural adaptability and wide absorption spectrum of PPy with boron's excellent thermal stability, chemical inertness, and affordability, resulting in a strong and scalable photothermal composite suitable for solar steam generation.[17] A mechanically stable scaffold for the photothermal layer is provided by a porous, flexible, and conductive substrate, such as cotton fabric, which promotes effective vapor escape.[18]

In this study, we present a novel radially symmetric photothermal evaporator that stands out for its synergistic chemical composition and distinctive floating architecture. An important innovation is the evaporator's circular shape, which facilitates even heat distribution and effective salt diffusion from the center to the periphery, reducing salt buildup and allowing for continuous operation in high-salinity brines. To provide a constant, omnidirectional water supply, this is integrated with a floatable, thermally insulating base made of hydrophobic PET foam, completely covered in hydrophilic cotton fabric. The boron–polypyrrole (B–PPy) composite is formed through interactions between boron species and the PPy matrix, creating a stable photothermal active layer. Such molecular-level synergy contributes to improved broadband light absorption and effective photothermal heat generation. Here, a homogenous slurry of boron and pre-synthesised PPy in dimethyl sulfoxide (DMSO) was prepared to create the photothermal layer. This slurry was then brush-coated onto a cotton fabric (CF) substrate to create a strong, flexible, and highly absorptive surface. The B–PPy@CF photothermal evaporator was then set up on top of the PET foam platform, which was covered with cotton. This integrated design reduces parasitic heat loss to the bulk water, efficiently restricts the heat generated at the evaporation interface, and maintains a steady flow of water through the cotton fabric. We systematically investigated the performance of this evaporator for solar-driven water evaporation under simulated sunlight, assessing its evaporation rate and energy conversion efficiency (Fig. 1). Additionally, the desalination of simulated seawater, which displayed good salt rejection and self-cleaning capabilities, as well as the removal of various metal ions (such as Ca^{2+} and Mg^{2+}) and common metal ions from polluted water, demonstrated the device's practical applicability. This work highlights a rational design of a low-cost, stable, and highly efficient photothermal system for sustainable freshwater production.

2. Experimental section

2.1 Materials

Pyrrole (C_4H_5N, 98%) was purchased from Sigma-Aldrich and distilled before use. Ammonium persulfate ($(NH_4)_2S_2O_8$, 98%) was obtained from Merck and used as an oxidizing agent. Amorphous boron (B, 99%) powder was acquired from Alfa Aesar. Dimethyl sulfoxide (C_2H_6OS, 99.5%) was supplied by Sigma-Aldrich. All chemicals were used as received without further purification. Polyethylene terephthalate ($C_{10}H_8O_4$) foam (thickness ~5 mm) was procured from a local supplier. Plain-woven, cotton fabric (mass per unit area ~120 g m^{-2}) was used as the substrate and water channel. Deionized H_2O was used throughout the experiments.

2.2 Fabrication of B/PPy@CF photothermal evaporator

The synthesis of polypyrrole (PPy) through chemical oxidation was the first step in the production process. Ammonium persulfate ($(NH_4)_2S_2O_4$) was used as the oxidant to polymerize pyrrole monomer (C_4H_2N) in a 1 M hydrochloric acid (HCl) medium. The resulting pure PPy powder was then thoroughly washed and dried. To create a homogenous suspension, amorphous boron powder was dispersed in dimethyl sulfoxide (C_2H_3OS) while being mechanically stirred. Subsequently, a cotton fabric substrate was evenly brush-coated with the boron dispersion. The same boron-coated fabric was then uniformly brush-coated with a solution of the produced PPy. To ensure that the composite layer adhered firmly to the cotton

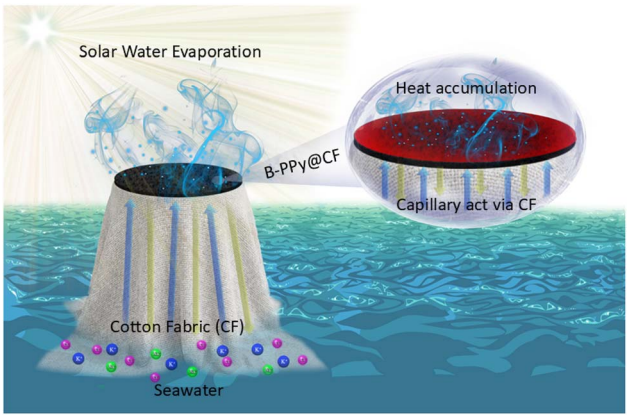

Fig. 1 Schematic illustration of a decoupled and scalable solar evaporator integrating boron-enhanced polypyrrole photothermal fabric for efficient water purification.

fibers and to eliminate any remaining solvent, the coated cloth was dried at 70 °C in an electric oven. The coated fabric was then crafted into a round-shaped evaporator. This technique produced the final B–PPy@cotton photothermal layer.

A hydrophobic polyethylene terephthalate (PET) foam was cut into a circular shape and fully wrapped with a different piece of pristine cotton fabric for the floating support structure. In addition to acting as an omnidirectional water transport channel that continuously supplies water from the bulk to the photothermal layer *via* capillary action, this cotton-wrapped PET foam also acts as thermal insulation to reduce heat loss to the underlying water. The entire solar evaporation setup is shown, with the B–PPy@CF photothermal evaporator placed on top of a cotton-wrapped PET foam floating support and a Petri dish filled with water. The B–PPy@CF layer effectively collects solar energy and transforms it into heat under simulated sunlight irradiation, producing visible steam at the surface. Fig. 2 also shows an infrared (IR) thermal image of the functioning device, which clearly shows effective heat localization at the photothermal evaporator surface, which, when illuminated, reaches a temperature of 39.7 °C. In order to minimize thermal losses to the surrounding bulk water and achieve high evaporation efficiency, this focused heating is essential.

2.3 Characterization

A Field Emission Scanning Electron Microscope (FESEM, JSM-7100F) was used to examine the surface morphology and microstructure of the manufactured B–PPy powder. For confirmation of the consistent deposition of boron and polypyrrole, the integrated Energy Dispersive X-ray (EDX) spectrometer was used to investigate the elemental composition and distribution over the fabric surface. Using a monochromatic Al Kα X-ray source on a Thermo Scientific Escalab 250Xi system, X-ray photoelectron spectroscopy (XPS) was applied to analyze the surface composition and chemical states of the B–PPy powder. Fourier-Transform Infrared (FTIR) spectroscopy was used to determine the presence of functional groups and the chemical interactions between boron and polypyrrole. Additionally, the heat localization efficiency of the evaporator was assessed by assessing the samples' thermal conductivity at room temperature using a transient plane source method with a thermal constant's analyzer.

2.4 Solar evaporation performance

Under standard laboratory settings (20 ± 2 °C, 50 ± 5% relative humidity), the solar-driven evaporation performance of the constructed device was assessed. AM 1.5G spectrum irradiation at 1 kW m^{-2} (1 sun intensity) was produced using a Class AAA solar simulator (PerfectLight, PLS-SXE300D). The final evaporator floated on the surface of the aqueous solutions, consisting of the round-shaped B–PPy@CF photothermal layer positioned on the cotton-wrapped PET foam support. Deionized (DI) water, with various weight percent NaCl solution to mimic saltwater, and artificial wastewater polluted with metal ions like Ca^{2+}, Mg^{2+}, Na^{+}, and K^{+} at 100 parts per million each were among the studied solutions. A high-precision analytical balance (Mettler Toledo, ME204/02) with a resolution of 0.1 mg was used to constantly record the mass change of the complete system in real-time. Data points were logged at 10-second intervals. To create a reliable thermal equilibrium baseline, the system was allowed to stabilize in the dark for half an hour before irradiation. The linear, steady-state mass loss observed during 60 minutes of continuous illumination was used to compute the evaporation rate. An infrared thermal camera (FLIR, E60) was used to record the evaporator's thermal performance and surface temperature distribution while it was operating. This technique allowed for the simultaneous monitoring of temperature profiles across the photothermal surface (B–

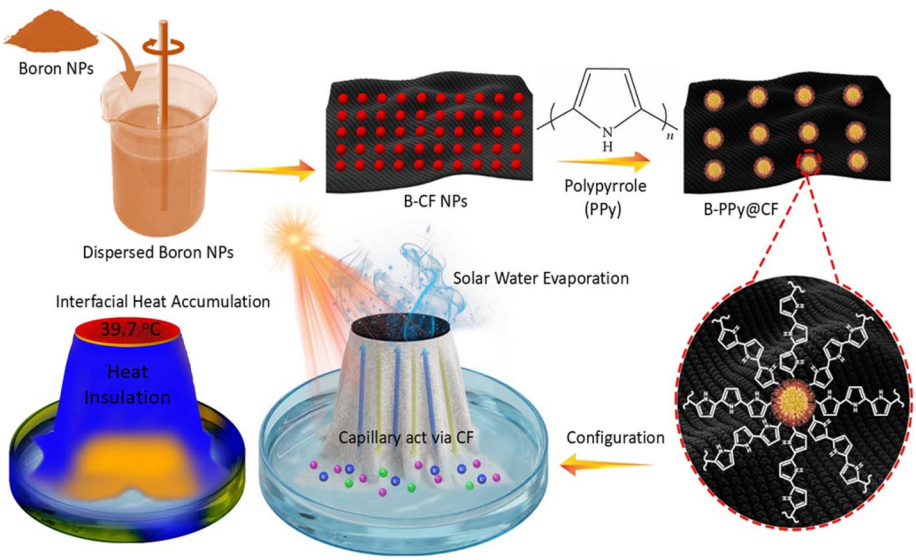

Fig. 2 Diagrammatic representation of the fabrication process of the B–PPy@CF photothermal evaporator and the assembly of the floating solar evaporation system, along with an infrared thermal image displaying surface temperature distribution under light.

PPy@CF), the underlying water-saturated cotton fabric, and the surrounding bulk water.

3. Results and discussion

3.1 Morphological analysis

The FESEM study of the manufactured B–PPy@CF photothermal evaporator and the immaculate cotton fabric is shown in Fig. 3. These morphological studies are essential for comprehending the substrate's surface properties and coating homogeneity, which have a direct impact on the device's overall evaporation performance, water transport, and light absorption. Fig. 3a–c depict the pure cotton fabric's surface morphology at increasingly higher magnifications. The FESEM images reveal that the clean cotton fibers exhibit a smooth and clean surface texture, which is characteristic of native cellulosic fibers after scouring and bleaching treatments. A naturally porous structure is created by the fibers' random and uneven interwoven network arrangement. Because they promote capillary action and offer several routes for water to reach the photothermal layer, cellulose's intrinsic porosity and hydrophilic properties are beneficial for water transport.[19] The FESEM pictures of the manufactured B–PPy@CF photothermal evaporator at various magnifications are shown in Fig. 3d–f.

The fiber surfaces exhibit notable morphological changes following the successive brush-coating of boron dispersion and polypyrrole solution. The images show that the cotton fibers have a consistent, thick layer of B–PPy compound. As is typical of polypyrrole-based coatings, where polymer chains tend to form clustered structures during the drying process, the composite has a rough and agglomerated granular morphology.[20,21] This B–PPy agglomeration on the fiber surfaces helps create a micro-scale rough architecture that improves light trapping through various scattering and reflection effects, increasing the evaporator's overall solar absorption capacity. Crucially, Fig. 3f shows that some porous configuration is preserved within the fiber network despite the deep covering. In order to ensure prolonged evaporation performance, avoid vapor trapping, and enable effective vapor escape throughout the evaporation process, this retained porosity is crucial.[22]

3.2 Chemical and structural characterization

The B–PPy composite powder's Fourier-transform infrared (FTIR) and X-ray photoelectron spectroscopy (XPS) analyses are shown in Fig. 4. Understanding the elemental composition, chemical states, and molecular interactions within the composite, all of which have a direct impact on the photothermal conversion efficiency and stability of the evaporator, requires these spectroscopic studies. The survey XPS spectra of the B–PPy composite powder are shown in Fig. 4a. The presence of boron, carbon, nitrogen, and oxygen elements in the composite is confirmed by the spectra, which show discrete photoelectron peaks corresponding to B 1s, C 1s, N 1s, and O 1s core levels. These peaks' existence confirms that the boron and polypyrrole components were successfully incorporated into the composite material. The B 1s region's high-resolution XPS spectrum are displayed in Fig. 4b.[23] The B 1s XPS spectrum shows a prominent peak located at 191.8 eV, indicative of boron species that are oxidized or coordinated with oxygen (B–O-related bonding). The lack of distinct multiple components indicates that boron mainly exists in a consistent chemical environment within the composite. Consequently, the analysis emphasizes the peak position and its chemical significance rather than breaking it down into several sub-peaks. Fig. 4c displays the high-resolution C 1s spectrum, which can be divided into two sub-peaks. The carbon atoms in C–C and C–H bonds, which come from the polypyrrole backbone and adventitious carbon, are responsible for the peak at 284.7 eV.[24] The existence of nitrogen-containing groups inside the polypyrrole structure and potential interactions with boron are indicated by the second peak at 287.0 eV, which represents carbon atoms bound to nitrogen or oxygen functionality (C–N/C–O). Three deconvoluted peaks can be seen in the high-resolution O 1s spectra shown in Fig. 4d. The signal at 531.7 eV is usually attributed to oxygen in hydroxide groups or carbonyl-type oxygen (C=O). Oxygen atoms in C–O–C or C–O–H

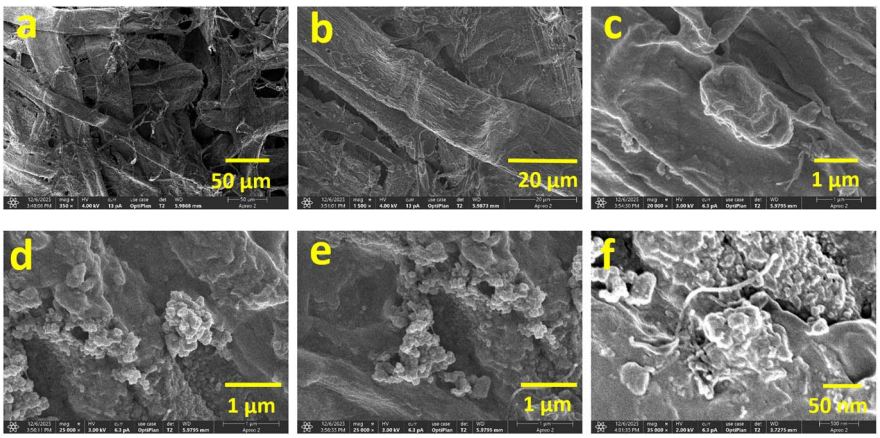

Fig. 3 (a–c) FESEM pictures of immaculate cotton fabric at various magnifications. (d–f) FESEM pictures of the B–PPy@CF photothermal evaporator at various magnifications.

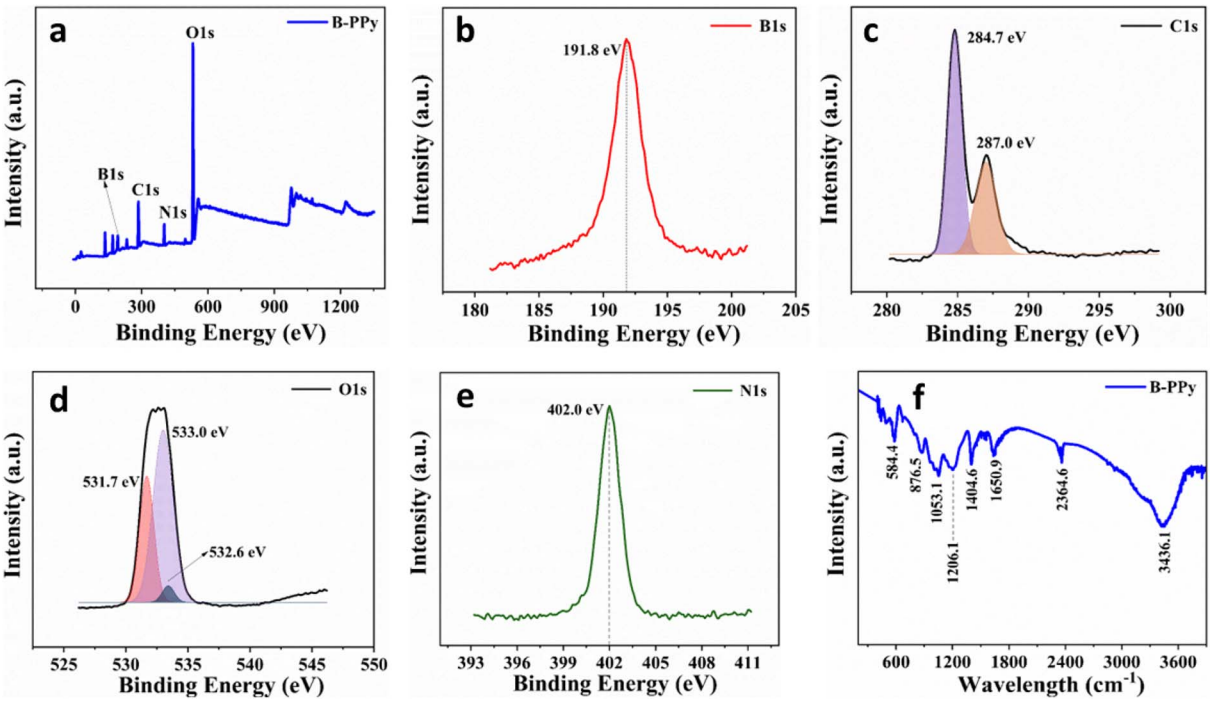

Fig. 4 (a) XPS survey spectrum of B–PPy composite powder displaying the presence of B 1s, C 1s, N 1s, and O 1s core levels. (b–e) High-resolution XPS spectrum of (b) B 1s, (c) C 1s, (d) O 1s, (e) N 1s. (f) FTIR spectrum of B–PPy composite powder.

configurations are represented by the component at 532.6 eV. Oxygen in adsorbed water molecules or ether-type connections is characterized by the peak at 533.0 eV. Several oxygen species indicate surface oxidation and the addition of functional groups containing oxygen during synthesis. A single symmetric peak at 402.0 eV is visible in the N 1s spectra displayed in Fig. 4e. This binding energy is particular to the positively charged nitrogen species (–N^{+}H–) in the oxidized state of polypyrrole and is characteristic of nitrogen atoms in the polypyrrole ring structure.[25] The structural integrity of the polypyrrole component following composite creation is confirmed by the lack of additional nitrogen peaks, which suggests a consistent chemical environment for nitrogen within the composite. The B–PPy composite powder's FTIR spectrum is shown in Fig. 4f. The FTIR analysis confirms the existence of boron-related bonding and its interaction with the polymer matrix. The bands detected at 584.4 and 876.5 cm^{-1} are ascribed to B–O/B–O–B vibrational modes. The peaks found at 1053.1, 1206.1, 1404.6, and 1650.9 cm^{-1} are linked to characteristic vibrations of the PPy backbone, such as C–N stretching and conjugated ring modes, suggesting that the incorporation of boron affects the local chemical environment of the polymer structure. Moreover, the broad band at 3436.1 cm^{-1} is related to O–H/N–H stretching vibrations, indicating the presence of surface hydroxyl groups or absorbed moisture, while the faint band at 2364.6 cm^{-1} corresponds to adsorbed CO_2. These combined spectroscopic findings indicate that the inclusion of boron modifies the local bonding configuration and the electronic structure of the.[26]

3.3 Heat localization and thermal response

The B–PPy@CF photothermal evaporator surface's time-dependent infrared (IR) thermal images under simulated solar irradiation at 1 kW m^{-2} (1 sun) are shown in Fig. 5. These thermal imaging studies are crucial for understanding the heat generation capability, heat localization efficiency, and thermal response time of the fabricated evaporator, which directly correlate with its solar-driven evaporation performance. The synergistic effect between boron and PPy can be understood from the perspective of bonding-state modulation, electronic structure regulation, and enhanced photothermal conversion pathways. This integration creates localized defect sites and polar bonding topologies, which affect the electrical structure of PPy by modifying charge distribution along the conjugated backbone.[27,28] As a result of greater electronic transitions and improved light–matter interaction, the material has better light absorption across a wider spectral range. Furthermore, the presence of boron-related species allows for a more effective conversion of absorbed photon energy into thermal energy, resulting in a stronger photothermal response.[29] Meanwhile, the PPy architecture offers a continuous conjugated network that enables efficient energy transfer and heat production. As a result, the synergistic interaction results from the combination of boron-induced bonding and electronic modulation with PPy's intrinsic conjugated structure, which leads to higher broadband absorption and photothermal conversion efficiency. The infrared images taken from the top surface of the B–PPy@CF evaporator at various intervals under continuous illumination are shown in Fig. 5a–h. The surface temperature was recorded at 25.2 °C at the beginning (0 minutes), which is the

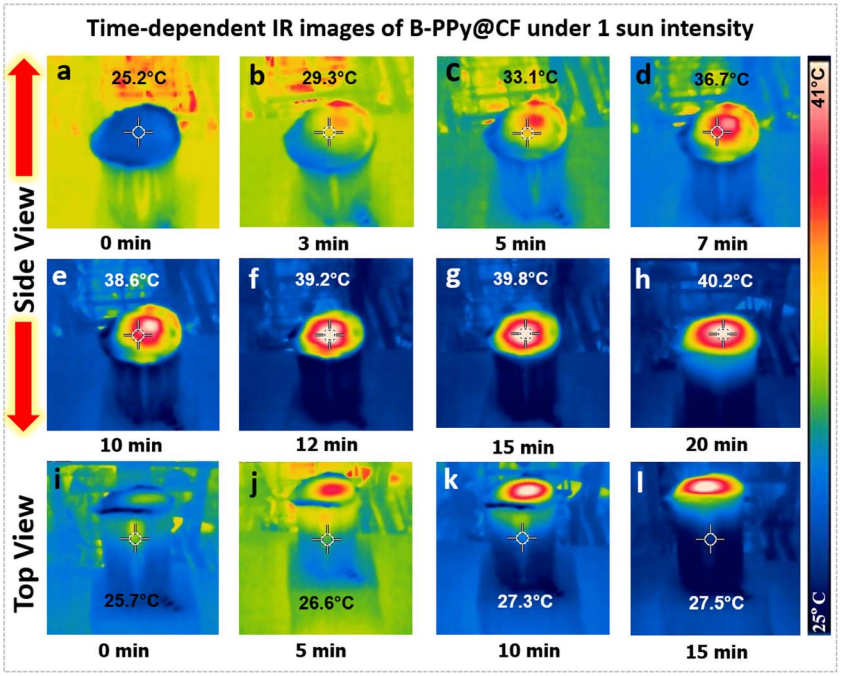

Fig. 5 (a–h) Time-dependent infrared thermal images of the top surface of the B–PPy@CF photothermal evaporator under 1 sun illumination (1 kW m^{-2}). (i–l) Infrared thermal images of the bottom surface of the B–PPy@CF evaporator under 1 sun illumination.

ambient temperature before exposure to light. The surface temperature rose quickly after irradiation. The B–PPy composite's exceptional photothermal conversion ability, which effectively absorbs incident solar light and transforms it into thermal energy, is demonstrated by this quick initial temperature rise. After 12 minutes, the temperature rose steadily to 39.2 °C. The device reached thermal equilibrium when the surface temperature stabilized at 40.2 °C after 20 minutes of continuous light. The B–PPy composite's effective light-to-heat conversion is confirmed by the accomplishment of a steadily rising temperature under one sun illumination, which is comparable to many recently reported photothermal evaporators.[30,31] The infrared pictures taken from the B–PPy@CF evaporator's bottom surface at 0, 5, 10, and 20 minutes under light are shown in Fig. 5i–l. The infrared (IR) thermal images indicate that the temperature of the bottom surface rises only from 25.7 °C to 27.5 °C after 20 minutes of operation. This slight increase in temperature demonstrates that there is limited heat transfer to the bulk water below. This behavior indicates that the B–PPy@CF evaporator has an effective insulating structure that minimizes conductive heat loss. As a result, heat is concentrated at the evaporation interface. This concentrated heating facilitates efficient water evaporation. Conductive heat transfer from the photothermal layer to the underlying bulk water is successfully reduced by the hydrophobic PET foam core wrapped in cotton fabric. Particularly noteworthy is the finding that the bottom temperature dropped to about 23.8 °C for the duration of the experiment after first rising slightly to 24.4 °C at 5 minutes. This behavior implies that the system reaches a dynamic thermal equilibrium in which there is little downward conduction and the heat produced at the top surface is efficiently contained and used for evaporation. As evaporation begins and consumes thermal energy at the interface, the tiny initial temperature increase may be the result of temporary heat diffusion that is later overcome by the creation of a steady-state temperature gradient. Instead of dissipating into the bulk water as parasitic heat loss, this thermal management method makes sure that the generated heat is mostly contained at the evaporation interface, where it is required for vapor formation. Because it minimizes the total energy input needed to reach the evaporation temperature and optimizes the use of the absorbed solar energy for phase change, the localized heating effect is crucial for attaining high energy efficiency in solar-driven evaporation systems. The B–PPy@CF evaporator successfully reduces parasitic heat loss, as evidenced by the small temperature increase at the bottom surface (just 2.6 °C above ambient after 20 minutes). This contributes to the evaporator's overall high performance and represents a major advancement in heat localization design.[32]

3.4 Evaporation rate and efficiency

The B–PPy@CF photothermal evaporator's solar-driven evaporation performance is shown in Fig. 6, along with mass change measurements under various circumstances and a comparison of evaporation rates and photothermal efficiencies. These findings are essential for measuring the manufactured device's capacity for evaporation and proving how well it addresses parasitic heat losses through effective heat localization. The experimental setup used to measure steam generation is shown in Fig. 6a. To track changes in mass in real time, the entire solar evaporator assembly, which included the B–PPy@CF

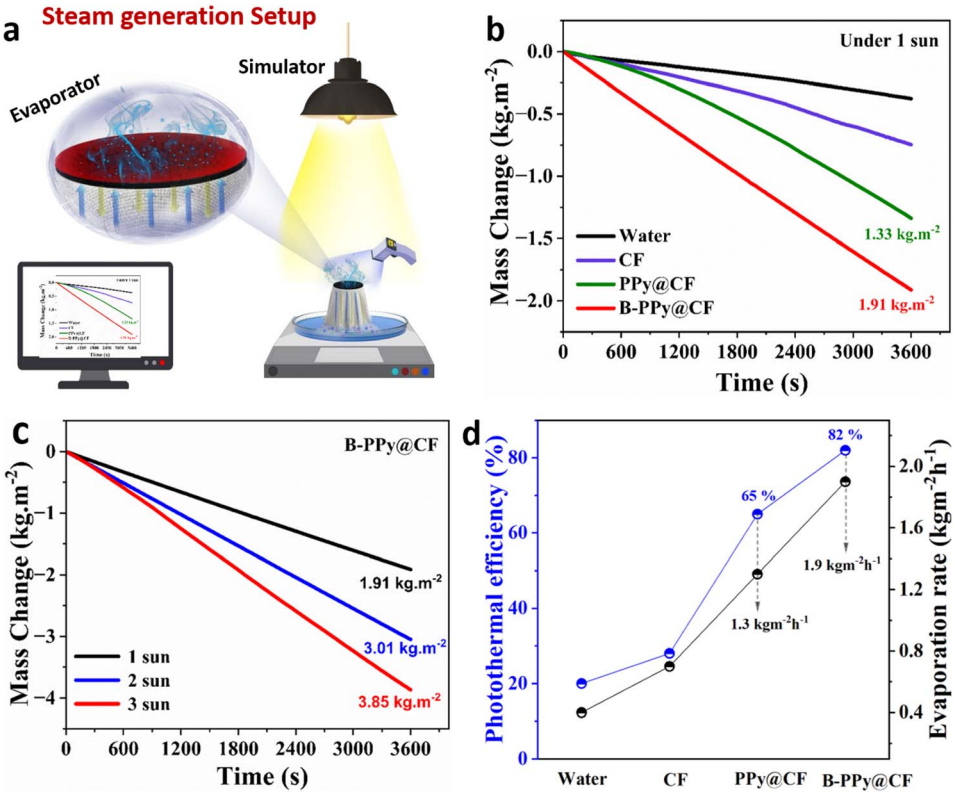

Fig. 6 (a) The experimental setup for measuring solar evaporation. (b) Time-dependent mass change of pure water, CF, PPy@CF, and B–PPy@CF evaporators under 1 sun illumination (c) time-dependent mass change of the B–PPy@CF evaporator under 1 sun, 2 sun, and 3 sun illumination over 3600 seconds. (d) Comparison of photothermal efficiency and evaporation rate for pure water, cotton fabric, PPy@CF, and B–PPy@CF evaporators under 1 sun illumination.

photothermal layer floating in water on a cotton-wrapped PET foam support, was placed on a high-precision analytical balance. The time-dependent mass change of four distinct samples, pure water (no evaporator), CF alone, PPy@CF, and the B–PPy@CF composite evaporator, under one sun illumination for 3600 seconds (one hour), is displayed in Fig. 6b.[33] Due to the lack of any photothermal material and substantial heat loss into the bulk water, the pure water sample showed the least amount of mass change, roughly 0.25 kg m^{-2}, during the entire period. Due to its hydrophilic character,[34] which facilitates water transport and some natural evaporation increase, the cotton fabric alone demonstrated an improved mass change of around 0.8 kg m^{-2}. The PPy@CF evaporator showed a significantly greater mass change of 1.33 kg m^{-2}, demonstrating polypyrrole's efficient photothermal conversion capabilities.[35] Surprisingly, the B–PPy@CF composite evaporator produced the largest mass change of 1.90 kg m^{-2}, which is much better than pure water and PPy@CF. The boron and polypyrrole composite's synergistic photothermal effect, which improves broadband light absorption and efficient heat generation, along with the heat localization design that reduces parasitic thermal losses to the underlying bulk water, is responsible for this superior performance. The B–PPy@CF evaporator's mass change over 3600 seconds at 1, 2, and 3 suns of solar light is shown in Fig. 6c. As solar intensity rose, the mass loss gradually increased, reaching 1.91 kg m^{-2} under 1 sun, 3.01 kg m^{-2} under two sun, and 3.85 kg m^{-2} under 3 suns.[36] The B–PPy@CF evaporator's exceptional responsiveness and scalability are demonstrated by this linear increase in evaporation with irradiation intensity, indicating that the photothermal evaporator can efficiently use greater energy inputs without performance loss. Stable heat localization even under concentrated illumination circumstances is indicated by the consistent performance across a range of solar intensities. The photothermal efficiency and evaporation rate for pure water, cotton fabric, PPy@CF, and B–PPy@CF under one sun's light are shown in Fig. 6d. The steady-state mass loss over time was used to calculate the evaporation rate. With a matching efficiency of roughly 20%, pure water showed the lowest evaporation rate of roughly 0.4 kg m^{-2} h^{-1}, indicating considerable heat losses to the bulk water and surrounding environment. Due to its larger surface area for evaporation, cotton fabric alone demonstrated a somewhat higher evaporation rate of 0.6 kg m^{-2} h^{-1} and efficiency of 27%. The PPy@CF evaporator demonstrated the efficient photothermal conversion of polypyrrole by achieving a significantly greater evaporation rate of 1.3 kg m^{-2} h^{-1} with 65% efficiency. With an exceptional photothermal efficiency of 82%, the B–PPy@CF evaporator achieved the maximum evaporation rate of 1.90 kg m^{-2} h^{-1}. The B–PPy@CF evaporator's high efficiency of 82% is especially noteworthy when it comes to

mitigating heat losses in solar-powered water evaporation. This value approaches the theoretical limits for interfacial evaporation systems and significantly surpasses that of many previously documented photothermal evaporators. The superior performance is attributed to the enhanced broadband light absorption of the B–PPy composite, the hydrophobic PET foam core's superior thermal insulation that reduces conductive heat loss to the bulk water, and the continuous water supply *via* capillary action through the cotton fabric that guarantees enough water at the evaporation interface without flooding the photothermal layer are all directly responsible for the superior performance. 82% efficiency validates the heat management technique used in this work by confirming that most of the absorbed solar energy is efficiently used for water vapor formation rather than being wasted as parasitic heat losses.

3.5 Performance in diverse water environments

The comparative analysis of surface temperature profiles of prepared evaporators under 1 kW m^{-2} illumination and the B–PPy@CF evaporator's evaporation performance under saline media are shown in Fig. 7. These studies are crucial for proving the manufactured device's exceptional heat localization capacity and its usefulness for actual water purification situations, such as desalination and wastewater treatment. The comparative surface temperature evolution of water, CF, PPy@CF, and B–PPy@CF under 1 sun illumination is presented in Fig. 7a. Pure water exhibits the lowest temperature (~21–22 °C), indicating negligible photothermal response. The CF substrate shows a slightly higher temperature (~26–27 °C), attributed to limited light absorption. Upon coating with PPy, the surface temperature increases significantly to ~35–36 °C, demonstrating enhanced photothermal conversion due to the conjugated polymer network. Notably, the B–PPy@CF sample achieves the highest temperature (40 °C), confirming further improvement after boron incorporation. The stable temperature profiles over time indicate steady-state thermal behavior. This progressive increase in surface temperature clearly demonstrates the synergistic effect of boron incorporation in enhancing light absorption and heat generation, which directly contributes to improved evaporation performance. The higher temperature rise demonstrates the synergistic photothermal effect of the boron–polypyrrole composite, leading to improved light absorption and heat generation. The time-dependent surface temperature profiles of the B–PPy@CF evaporator under one, two, and three suns irradiation is shown in Fig. 7b.

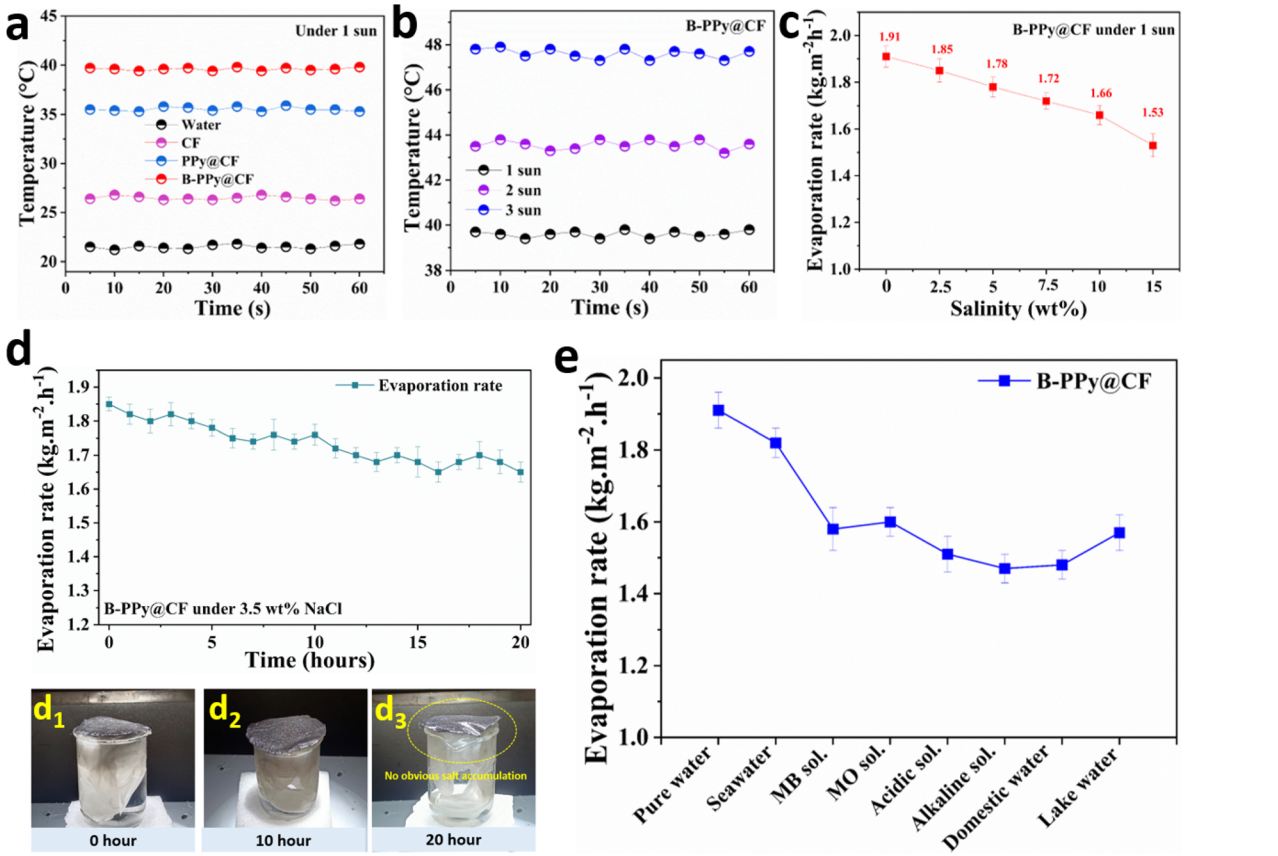

Fig. 7 (a) Time-dependent surface temperature profiles of pure water, CF, PPy@CF, and B–PPy@CF evaporators under 1 sun illumination. (b) Time-dependent surface temperature profiles of the B–PPy@CF evaporator under 1 sun, 2 sun, and 3 sun illumination. (c) Evaporation rates of the B–PPy@CF evaporator in various types of water. (d) Evaporation performance of B–PPy@CF under 3.5 wt% NaCl. (d_1–d_3) Digital images of the B–PPy@CF at 0, 10, and 20 h. (e) Evaporation rates of the B–PPy@CF evaporator in NaCl solutions with varying salinity from 0 to 15 weight percent.

The equilibrium temperature increased to around 44 °C when the illumination intensity was raised to 2 suns, and it reached about 48 °C under three suns. The B–PPy@CF evaporator's exceptional responsiveness and scalability are demonstrated by this gradual temperature increase with increased solar flux, indicating that the photothermal composite can efficiently use higher energy inputs without saturation. With little heat dispersion to the surrounding environment or bulk water, the constant temperature plateau at each intensity also shows steady heat localization even under intense lighting. The B–PPy@CF evaporator's evaporation rates in a variety of water types, pure water, saltwater, methyl orange and methylene blue solutions, acidic and alkaline solutions, household water, and lake water, are shown in Fig. 7c. In pure water, the evaporator reached its maximum evaporation rate of about 1.95 kg m^{-2} h^{-1}, which is in line with the findings displayed in Fig. 6. The evaporator's efficacy for desalination applications was demonstrated by the high evaporation rate in simulated seawater, which was around 1.80 kg m^{-2} h^{-1}. The lower vapor pressure of saline solutions, because of the dissolved salts, is responsible for the slightly lower rate when compared to pure water. Furthermore, the long-term performance of the evaporator was tested in a 3.5 wt% saline solution for continuous 20 hours, with the evaporation rate continually monitored. As seen in the time-dependent graph (Fig. 7d), the evaporation rate remained nearly constant throughout the testing period, indicating steady performance with no substantial decline. This consistency indicates that salt formation at the evaporation contact is successfully reduced over lengthy operation. To support this finding, photographs of the evaporator surface were taken at 0, 10, and 20 hours (Fig. 7d_1–d_3). Even after continuous operation, no visible salt crystallization or accumulation was observed on the surface. This can be attributed to the structure's effective water movement and salt dispersion, which avoids salt accumulations in specific areas. These findings affirm the remarkable resistance to salt and the enduring operational stability of the evaporator when subjected to saline environments. The evaporator performed well in treating wastewater contaminated with dyes, maintaining evaporation rates of approximately 1.58 kg m^{-2} h^{-1} for methylene blue and 1.60 kg m^{-2} h^{-1} for methyl orange in organic dye solutions. The evaporation rates were approximately 1.53 kg m^{-2} h^{-1} in acidic settings and 1.50 kg m^{-2} h^{-1} in alkaline conditions, indicating the B–PPy composite's chemical stability throughout a broad pH range. The evaporator produced rates of approximately 1.51 kg m^{-2} h^{-1} in household wastewater and 1.40 kg m^{-2} h^{-1} in lake water. The existence of several pollutants that can impact water activity and heat transmission is the reason for the slightly reduced performance in complicated real-world water matrices. Nonetheless, the B–PPy@CF evaporator's resilience and practical application for a variety of water purification scenarios are confirmed by the consistently high evaporation rates across all water types. The B–PPy@CF evaporator's evaporation rates in NaCl solutions with salinities ranging from 0 to 15 weight percent are shown in Fig. 7e. The rate of evaporation was 1.90 kg m^{-2} h^{-1} in pure water (0% NaCl). The evaporation rate dropped to 1.85 kg m^{-2} h^{-1} when salinity rose to 2.5 wt%. The rate was 1.78 kg m^{-2} h^{-1} at 5.0 wt% NaCl and 1.72 kg m^{-2} h^{-1} at 7.5 wt%. The evaporator maintained a decent rate of 1.53 kg m^{-2} h^{-1} even at the highest tested salinity of 15 wt%. The lower vapor pressure of high-concentration brine solutions and the higher energy needed for water evaporation in the presence of dissolved ions are responsible for the well-documented phenomenon of the steady decrease in evaporation rate with increasing salinity. Nevertheless, even at 15 weight percent salinity, the B–PPy@CF evaporator retains more than 80% of its initial evaporation rate, demonstrating exceptional salt tolerance. Two main factors contribute to this exceptional performance: (1) the radial symmetry of the round-shaped evaporator encourages uniform salt diffusion from the center to the edges, preventing localized salt accumulation and maintaining a continuous water supply; and (2) the effective heat localization at the evaporation interface guarantees sufficient thermal energy for vapor generation even in high-salinity environments. For practical desalination applications, especially when treating high-salinity brines or attaining high water recovery ratios, the capacity to maintain high evaporation rates in hypersaline conditions is essential.

3.6 Durability, outdoor performance, and desalination

The B–PPy@CF photothermal evaporator's real-time evaporation visualization, long-term cyclic stability, outdoor performance assessment, and water purification capacity are shown in Fig. 8. These studies are essential for demonstrating the manufactured device's utility, robustness, and potential for sustained freshwater production *via* effective heat-localized solar evaporation. An actual photo of the evaporation setup taken from the side is shown in Fig. 8a, and the equivalent front view of the evaporation chamber is shown in Fig. 8a_1. The efficient vapor production capabilities of the B–PPy@CF evaporator under illumination can be directly observed in Fig. 8a_1, where dense steam creation is clearly apparent inside the evaporation chamber. Rather than dissipating as parasitic heat loss to the surrounding environment or bulk water, the visible steam cloud verifies that the heat produced at the photothermal interface is efficiently used for vaporizing water. The B–PPy composite's exceptional photothermal conversion efficiency and the efficacy of the heat-localization design are demonstrated by the continuous steam generation observed under one-sun illumination without optical concentration. The evaporation rate of the B–PPy@CF evaporator for 15 consecutive cycles, each lasting one hour under one solar illumination, is shown in Fig. 8b. Throughout all 15 cycles, the evaporation rate was impressively constant at about 1.90 kg m^{-2} h^{-1}, with just a little variation noted. This exceptional cycle stability shows that the B–PPy@CF evaporator has high photothermal durability and structural integrity, with no performance loss or composite coating deterioration even after extended and frequent usage. With the PET foam insulation retaining its thermal management qualities and the cotton fabric continuing to provide water continuously through capillary action, the steady evaporation rate further demonstrates that the heat localization mechanism is still efficient over time. For real-

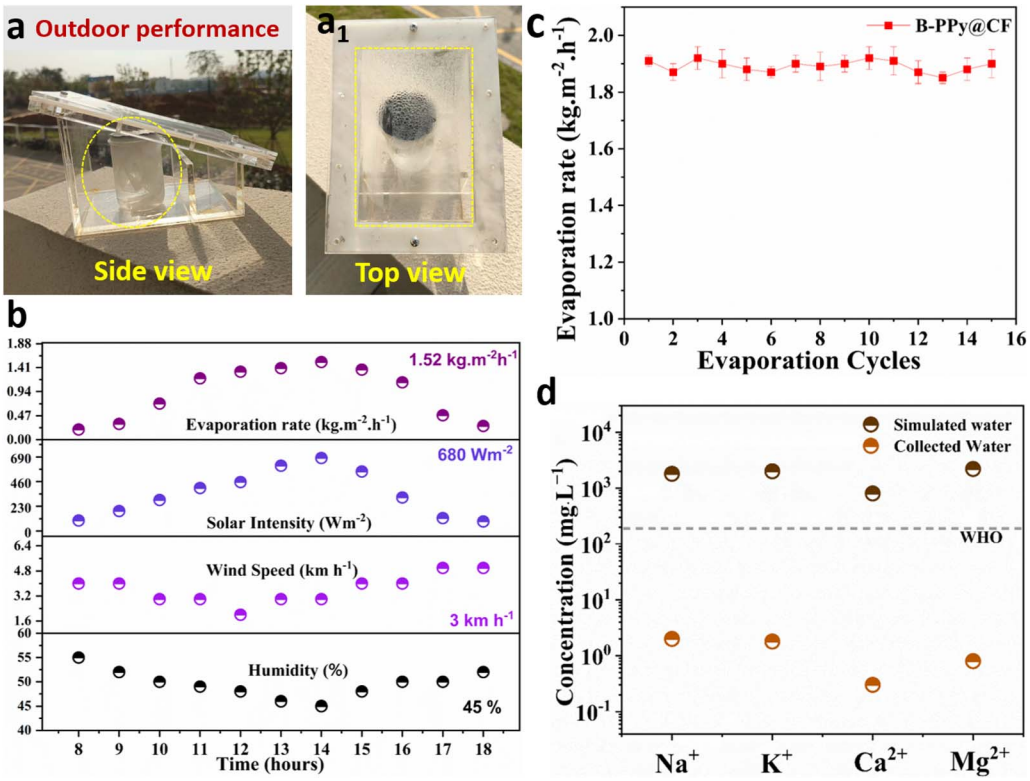

Fig. 8 (a) Real pictures of the evaporation setup from side view, and (a_1) front view of the evaporation chamber with visible steam generation. (b) Cyclic stability of the B–PPy@CF evaporator displaying an evaporation rate over 15 consecutive cycles under 1 sun illumination. (c) Outdoor performance evaluation showing variations in humidity, wind speed, solar intensity, and corresponding evaporation rate of the B–PPy@CF evaporator. (d) Concentration of Na^+, K^+, Ca^{2+}, and Mg^{2+} ions in simulated seawater and collected water using the B–PPy@CF evaporator.

world applications where continuous or daily cycle operation is necessary, such long-term stability is crucial. The B–PPy@CF evaporator's outdoor performance evaluation, which took place from 8:00 AM to 6:00 PM, is shown in Fig. 8c. It displays the changes in humidity, wind speed, sun intensity, and associated evaporation rate over the course of the day. The evaporation rate was about 0.2 kg m^{-2} h^{-1} at 8:00 AM with sun intensity of about 115 W m^{-2}, humidity at 55%, and wind speed of 4.0 km h^{-1}. As the day went on, humidity dropped to 45% and wind speed reduced to about 3.0 km h^{-1}, while sun intensity progressively increased and peaked at about 680 W m^{-2} at 2:00 PM. As a result, the rate of evaporation rose gradually and peaked at 2:00 PM at about 1.52 kg m^{-2} h^{-1}. The evaporation rate steadily dropped after 2:00 PM due to changes in wind speed, humidity, and sun intensity. By 6:00 PM, it had returned to roughly 0.2 kg m^{-2} h^{-1}. The B–PPy@CF evaporator efficiently uses available solar radiation for water vapor formation, as demonstrated by the excellent correlation between evaporation rate and solar intensity throughout the day. Considering the lower peak intensity, the impressive peak evaporation rate of 1.52 kg m^{-2} h^{-1} attained in natural sunlight (680 W m^{-2}) is comparable to the performance seen under simulated 1 sun circumstances (1.90 kg m^{-2} h^{-1} at 1000 W m^{-2}). The impact of environmental variables like humidity and wind speed can be attributed to the little deviations from a perfect match with sun intensity. While wind speed influences convective heat and mass transport at the surface, higher humidity somewhat suppresses evaporation by lowering the vapor pressure difference between the evaporator surface and the surrounding air. The B–PPy@CF evaporator's practical applicability for real-world solar desalination applications under variable climatic circumstances is confirmed by its effective outdoor operation. The ion concentration measurement of simulated seawater before and after purification using the B–PPy@CF evaporator is shown in Fig. 8d, along with a comparison with the acceptable limits set by the World Health Organization (WHO). Na^+, K^+, Ca^{2+}, and Mg^{2+} contents in the simulated seawater were approximately 3200 mg L^{-1}, 3210 mg L^{-1}, 2800 mg L^{-1}, and 3300 mg L^{-1}, respectively. The ion concentrations in the collected water were significantly lowered to about 1.2 mg L^{-1} for Na^+, 1.15 mg L^{-1} for K^+, 0.5 mg L^{-1} for Ca^{2+}, and 0.9 mg L^{-1} for Mg^{2+} using a single-step solar evaporation and condensation procedure utilizing the B–PPy@CF evaporator. The remarkable desalination capacity of the evaporator is demonstrated by these data, which equate to ion rejection rates surpassing 99.9% for all tested ions. The quantities of all ions in the filtered water are remarkably lower than the WHO acceptable limits for drinking water, which are normally 200 mg L^{-1} for Na^+, 200 mg L^{-1} for K^+, 75 mg L^{-1} for Ca^{2+}, and 50 mg L^{-1} for Mg^{2+}. Since only water molecules evaporate and all non-volatile solutes remain behind, the almost total elimination of these common metal ions demonstrates that the solar vapor generation process creates

high-purity water. The B–PPy coating's chemical stability and non-leaching properties, which are crucial for the manufacture of clean drinking water, are further supported by the photothermal composite's lack of contamination. The B–PPy@CF evaporator is a very promising and workable solution for sustainable freshwater production through solar-driven desalination and wastewater treatment because of its remarkable water purification performance, effective heat localization, and high evaporation rates shown throughout this study.

4. Conclusion

In this work, we successfully fabricated a novel, radially symmetric B–PPy@CF photothermal evaporator with an integrated floating thermal insulation platform for efficient solar-driven water evaporation. By limiting heat at the evaporation interface and ensuring a constant water supply through capillary action, the strategic design that combined a hydrophobic PET foam core with hydrophilic cotton fabric successfully solved the crucial issue of parasitic heat loss. The B–PPy evaporator demonstrated synergistic photothermal effects that improved broadband light absorption and effective heat generation. The B–PPy@CF evaporator achieved an outstanding evaporation rate of 1.90 kg m^{-2} h^{-1} with a high photothermal efficiency of 82% under 1 sun illumination. With a remarkable 15.9 °C temperature difference between the top (39.7 °C) and bottom (23.8 °C) surfaces at equilibrium, infrared thermal imaging confirmed exceptional heat localization, confirming minimal parasitic heat loss to the bulk water and validating the excellent thermal insulation provided by the PET foam core. The evaporator's ability to maintain high evaporation rates in seawater, organic dye solutions, acidic and alkaline environments, and actual water samples was impressive. During outdoor testing, the device demonstrated exceptional cyclic stability over 15 consecutive cycles, reaching a peak evaporation rate of 1.52 kg m^{-2} h^{-1}. Most significantly, with >99.9% rejection of Na^+, K^+, Ca^{2+}, and Mg^{2+} ions, the filtered water satisfied WHO drinking water requirements. This work offers a viable solution for sustainable wastewater treatment by presenting a scalable and highly efficient photothermal system that effectively handles heat losses in solar-driven evaporation.

Conflicts of interest

The authors declare no competing interests.

Data availability

Data available on request from the authors.

Acknowledgements

The authors extend their appreciation to the Deanship of Scientific Research and Libraries in Princess Nourah bint Abdulrahman University for funding this research work through the Research Group project, grant no. (RG-1445-0047).

References

1 H. Pltonykova, S. Koeppel, F. Bernardini, S. Tiefenauer-Linardon, L. de Strasser and R. Connor, *The United Nations World Water Development Report 2020: Water and Climate Change*, 2020.
2 C. A. Dieter, *Water Availability and Use Science Program: Estimated Use of Water in the United States in 2015*, Geological Survey, 2018.
3 A. J. Toth, Modelling and optimisation of multi-stage flash distillation and reverse osmosis for desalination of saline process wastewater sources, *Membranes*, 2020, **10**, 265.
4 N. A. A. Qasem, R. H. Mohammed and D. U. Lawal, Removal of heavy metal ions from wastewater: a comprehensive and critical review, *npj Clean Water*, 2021, **4**, 36.
5 Y. Sun, X. Tan, X. Yuan and J. Li, Solar-driven interfacial evaporation: Research advances in structural design, *Chem. Eng. J.*, 2024, 153316.
6 K.-F. Chang, Y.-Z. Li, J.-L. Xu and Y. Zhang, Key technology developments for solar-driven interface evaporation on structural innovation and thermal design, *Nano Energy*, 2024, **132**, 110369.
7 R. V. S. Madhuri, Z. Said, I. Ihsanullah and R. Sathyamurthy, Solar energy-driven desalination: A renewable solution for climate change mitigation and advancing sustainable development goals, *Desalination*, 2025, 118575.
8 C. Biswas and Y. H. Lee, Graphene versus carbon nanotubes in electronic devices, *Adv. Funct. Mater.*, 2011, **21**, 3806–3826.
9 S. Rikhtehgaran and A. Lohrasebi, Water desalination by a designed nanofilter of graphene-charged carbon nanotube: A molecular dynamics study, *Desalination*, 2015, **365**, 176–181.
10 K. Khurana and N. Jaggi, Localized surface plasmonic properties of Au and Ag nanoparticles for sensors: a review, *Plasmonics*, 2021, **16**, 981–999.
11 D. Wu, C. Zhao, Y. Xu, X. Zhang, L. Yang, Y. Zhang, Z. Gao and Y.-Y. Song, Modulating solar energy harvesting on TiO2 nanochannel membranes by plasmonic nanoparticle assembly for desalination of contaminated seawater, *ACS Appl. Nano Mater.*, 2020, **3**, 10895–10904.
12 D. Yang, B. Zhou, G. Han, Y. Feng, J. Ma, J. Han, C. Liu and C. Shen, Flexible transparent polypyrrole-decorated MXene-based film with excellent photothermal energy conversion performance, *ACS Appl. Mater. Interfaces*, 2021, **13**, 8909–8918.
13 Y. Kong, Y. Gao, B. Gao, Y. Qi, W. Yin, S. Wang, F. Yin, Z. Dai and Q. Yue, Tubular polypyrrole enhanced elastomeric biomass foam as a portable interfacial evaporator for efficient self-desalination, *Chem. Eng. J.*, 2022, **445**, 136701.
14 L. Lan, Y. Li, F. Zhou, F. Zhao, F. Wang, Z. Zhang, L. Wang and J. Mao, Self-supported polypyrrole sponge with photothermal–adsorption synergy for integrated water purification, *Sep. Purif. Technol.*, 2025, 135119.
15 C. Gao, Y. Li, L. Lan, Q. Wang, B. Zhou, Y. Chen, J. Li, J. Guo and J. Mao, Bioinspired asymmetric polypyrrole membranes

with enhanced photothermal conversion for highly efficient solar evaporation, *Adv. Sci.*, 2024, **11**, 2306833.

16 J. F. Thümmler, F. G. Golmohamadi, D. Schöffmann, J. Laufer, H. Lucas, J. Kollan, K. Mäder and W. H. Binder, Photo-thermoresponsive polypyrrole-crosslinked single-chain nanoparticles for photothermal therapy, *Commun. Chem.*, 2025, **8**, 124.

17 B. Yang, Y. Feng, W. Wang, M. Zhang, X. Kong, Q. Liu, H. Xu, J. Yao, G. Li and S.-Q. Guo, Interface engineering of amorphous boron for high-efficiency interfacial solar steam generation, *New J. Chem.*, 2023, **47**, 1059–1065.

18 H.-Y. Zhao, J. Zhou, Z.-L. Yu, L.-F. Chen, H.-J. Zhan, H.-W. Zhu, J. Huang, L.-A. Shi and S.-H. Yu, Lotus-inspired evaporator with janus wettability and bimodal pores for solar steam generation, *Cell Rep. Phys. Sci.*, 2020, **1**, 100074.

19 Y. Chen, X. Wu, J. Wei and H. Wu, Characterization and application to fiber reinforced composite of catechol/polyethyleneimine modified polyester fabrics by mussel-inspiration, *Fibers Polym.*, 2020, **21**, 2625–2634.

20 L. Zhu, L. Wu, Y. Sun, M. Li, J. Xu, Z. Bai, G. Liang, L. Liu, D. Fang and W. Xu, Cotton fabrics coated with lignosulfonate-doped polypyrrole for flexible supercapacitor electrodes, *RSC Adv.*, 2014, **4**, 6261–6266.

21 V. Jangra, P. Vishnoi and S. Maity, A comparative study of thermoelectric properties of various polypyrrole-coated textiles, *Fibers Polym.*, 2024, **25**, 2629–2645.

22 X. Wang, D. Yang, X. An and X. Qian, Phytic acid doped polypyrrole as a mediating layer promoting growth of prussian blue on cotton fibers for solar-driven interfacial water evaporation, *Polymers*, 2021, **14**, 6.

23 D. Schild, S. Ulrich, J. Ye and M. Stüber, XPS investigations of thick, oxygen-containing cubic boron nitride coatings, *Solid State Sci.*, 2010, **12**, 1903–1906.

24 J. Tabačiarová, M. Mičušík, P. Fedorko and M. Omastová, Study of polypyrrole aging by XPS, FTIR and conductivity measurements, *Polym. Degrad. Stab.*, 2015, **120**, 392–401.

25 M. Šetka, R. Calavia, L. Vojkůvka, E. Llobet, J. Drbohlavová and S. Vallejos, Raman and XPS studies of ammonia sensitive polypyrrole nanorods and nanoparticles, *Sci. Rep.*, 2019, **9**, 8465.

26 N. Su, H. B. Li, S. J. Yuan, S. P. Yi and E. Q. Yin, Synthesis and characterization of polypyrrole doped with anionic spherical polyelectrolyte brushes, *Express Polym. Lett.*, 2012, **6**, 697–705.

27 C. Ma, H. Guan, L. He, C. Ge, H. Yang and X. Zhang, Enhanced photothermal conversion efficiency by loading polypyrrole nanoparticles on the surface of boron nitride, *Mater. Lett.*, 2022, **324**, 132679.

28 C. Ma, L. He, R. Liu, H. Guan, C. Ge and X. Zhang, Preparation of Polypyrrole/Boron Nitride Composites and Composite Sponges for Efficient Photothermal Utilization, *ChemistrySelect*, 2022, **7**, e202201244.

29 F. Wang, Y. Zhang, B. Jiang, M. Cong, T. Shu, Y. Qin, Y. Lei and L. Dong, Photothermal Superhydrophobic Coating Based on Polypyrrole-Modified Boron Nitride with Exceptional Anti-Icing and Deicing Performance, *ACS Appl. Eng. Mater.*, 2023, 2635–2648.

30 B. Shakoor, X. Fan, R. Shi, N. Arshad, M. Alomar, I. Ahmed, M. Zeeshan, M. A. Ali, H. Razzaq and U. Ghazanfar, Architecting scalable polyelectrolyte wicking fabric for efficient and continuous salt-tolerant solar evaporation, *Sep. Purif. Technol.*, 2026, 137383.

31 D. Hao, Y. Yang, B. Xu and Z. Cai, Efficient solar water vapor generation enabled by water-absorbing polypyrrole coated cotton fabric with enhanced heat localization, *Appl. Therm. Eng.*, 2018, **141**, 406–412.

32 J. Tao, Z. Feng, S. Zhai, S. Huang, E. Yi, F. Zhu, L. Lin, J. Qian, M. S. Irshad and X. Wang, Side structural regulation strategy of 3D gear evaporators for enhanced solar water evaporation and salt harvesting, *Desalination*, 2025, 119206.

33 X. Li, G. Ni, T. Cooper, N. Xu, J. Li, L. Zhou, X. Hu, B. Zhu, P. Yao and J. Zhu, Measuring conversion efficiency of solar vapor generation, *Joule*, 2019, **3**, 1798–1803.

34 X. Min, B. Zhu, B. Li, J. Li and J. Zhu, Interfacial Solar Vapor Generation: Materials and Structural Design, *Acc. Mater. Res.*, 2021, 198–209.

35 G. Zhu, D. Kremenakova, Y. Wang and J. Militky, Temperature changes of plain cotton fabric during liquid absorption process, *Int. J. Cloth. Sci. Technol.*, 2015, **27**, 600–606.

36 L. Fan, C. Wei, Q. Xu and J. Xu, Polypyrrole-coated cotton fabrics used for removal of methylene blue from aqueous solution, *J. Text. Inst.*, 2017, **108**, 1847–1852.